A Study of Three-Phase Fracturing in Granular Media using High-speed Imaging

Deren Ozturk, Bjørnar Sandnes*
College of Engineering, Swansea University, Bay Campus, Fabian Way, Swansea SA1 8EN, UK.

Using high-speed imaging and digital image correlation, we study the granular motion and deformation caused by pneumatic fracturing of a wet granular packing in a Hele-Shaw cell subject to a constant injection of air. These pneumatic fractures form patterns of conductive pathways whose form is determined by a complex interplay between pressure, capillary, frictional, and viscous forces. Saturated granular media is pneumatically fractured in this fashion in multiple natural, geo-engineering, and industrial processes. We outline the characteristics of these fracture networks and then examine individual fracture growth events and the local motion of grains with a time resolution of milliseconds. We observe intermittent frictional behaviour during these rapid fracturing events, describe an average velocity profile for the motion of grains during fracturing, and illustrate an average compaction profile as a result of these deformations.

INTRODUCTION

Gas-driven fracturing of liquid-saturated granular media, also referred to as pneumatic or capillary fracturing, occurs in numerous natural, geo-engineering, and industrial processes. In nature for example, these fracturing processes influence methane venting in sediments at the ocean floor, outgassing in crystal-rich volcanic magma, and soil drying or cracking (see e.g. [13, 18, 21, 29, 30]). In geo-engineering, pneumatic fracturing can be used in soil remediation to increase the permeability of a soil to more efficiently treat hazardous contaminants (e.g. [7, 12]). While in industry it is relevant to carbon dioxide injection storage and the stimulation of sensitive hydrocarbon reservoirs ([3, 22]).

The granular fracturing that is discussed in this and other similar works is distinctly different from the typical fracturing involving the breaking of cohesive bonds in a continuously solid material, such as in hydraulic fracturing of shale rock, also known as ”fracking”. Instead, there are no cohesive bonds between grains in granular fracturing, the fracture cavity that develops is caused by a gas mobilising and displacing the interstitial fluid and grains. Three-phase flow involves a complex interplay of pressure, frictional, capillary, and viscous forces and doesn't just produce fracturing, but a wide variety of other phenomena and pattern morphologies (see e.g. [19, 24–26]).

To enable detailed observation of the complex fracture growth process, a quasi-two-dimensional system, a Hele-Shaw cell, is often used to image the evolving invasion patterns ([14, 23]). Many experiments have used a Hele-Shaw cell to examine fluid flow in granular materials in varying setups. If the granular material is compact and fixed in place then capillary invasion occurs between the grains as the gas is injected at a low rate, while the well-studied instability of viscous fingering is observed at high injection rates (e.g. [20, 28]). If the granular material is loose, and the granular material only partly fills the cell, then the invasion of gas can result in a wide variety of patterns, including frictional fingers, stick-slip bubbles and coral-like structures ([19, 24–26]). The regime of fracturing studied here lies between those two setups: the gap in the Hele-Shaw cell is initially fully occupied by a packing of water-saturated granular material, however the packing is not so tight that the grains cannot move, allowing for deformation. The slow invasion of a gas under these conditions results in growth of narrow branches resembling fractures.

A number of studies have previously observed multiphase fracturing (see e.g. [4, 6, 10, 11, 16, 17, 24, 27]). Fracture patterns were observed transitioning from viscous fingering in dense granular suspensions ([5]), and then later mapped and explained as resulting from the capillary forces overcoming the frictional resistance of the granular media ([15, 16]). In a recent study, [2] showed that the fractures branch out to form a bifurcating network with a characteristic spacing between the fracture branches. The influence of grain size, shape and gas injection rate was studied, and a simple model was presented that predicted the spatial fracture density based on the properties of the granular material and fluids.

Here we introduce new insights into the motion of the packing at the granular scale during individual fracturing events. We first present an example of the multiphase fracture patterns formed in a Hele-Shaw cell and illustrate the stick-slip nature of the growth process on a time-scale of minutes. We then use a high-speed camera and image analysis to examine the motion of the fracture and its surrounding grains. The high-speed imaging revealed additional frictional intermittent behaviour at significantly shorter time-scales, and allowed us to use Particle Image Velocimetry (PIV) to calculate displacement, velocity, and compaction fields for the deformation of the granular packing surrounding the growing fracture. We used data from multiple fracturing events to generate an average velocity profile of fracture growth for the system, as well as a subsequent average compaction profile. These profiles help explain many of the interesting features of multiphase fracture patterns, including how local granular compaction induces stick-slip behaviour and creates a compacted zone surround the fractures that other fractures cannot penetrate, determining the characteristic spacing between them.

MATERIALS AND METHODS

Fracture Pattern Generation

The branching fracture patterns presented here were created in experiments using a Hele-Shaw cell, see Figure 1. Impermeable adhesive plastic spacers were used to hold two 350x350x18 mm^3 glass plates apart, creating a 200 mm wide, 300 mm long channel with a 0.5 mm gap height. One end of the cell was open to the surrounding atmosphere, and a hole for an inlet was drilled 300 mm from the open end. See [2] for a more detailed description of this setup.

The cell was filled with water-saturated, loosely packed spherical soda-lime glass beads, sieved to a size range of 0.20–0.25 mm. The cell was filled by turning it vertical, flooding it with deionised water and then pouring in grains quickly and evenly across the channel width, ensuring the cell was constantly filled with gradually settling grains. The grains were filled up to 10 mm below the open end of the channel, with the remaining space filled with water, preventing evaporation from affecting the granular packing during the experiment.

Once the bed had settled the cell was turned horizontal. A syringe pump (Harvard Scientific, PHD Ultra) was used to inject air through the cell inlet into the water-saturated granular packing confined in the cell gap. The pressure of the air was recorded at 5 Hz during injection with a difference pressure sensor (Sensortechnics DC13) connected to a National Instrument-9171 analogue input DAQ module. The air was injected at a rate of $Q_{\text{pump}} = 0.01$ ml.min^{-1} from an air reservoir of $V_{\text{gas}} = 8$ ml contained within a syringe. The development of the fracture pattern was photographed with a camera (Nikon J2) every 20 s with an image resolution of 3872x2592 pixel^2. Typically the experiment would run for up to 30 minutes as the fracture pattern explored the cell until it reached the end of the packing near the cell opening.

Prior to use, the beads were washed in a 3:1 mix of sulphuric acid and hydrogen peroxide and then rinsed in deionized water to ensure clean hydrophilic surfaces with an estimated air-water-glass contact angle of $\theta = 12 \pm 5°$ ([8]). The filling procedure and gentle sedimentation ensured that the beads were loosely packed and that the packing was deformable. The bead beds had an estimated porosity of $n = 0.47$, which is concordant with the expected values for a random loose packing of spheres ([9]). The large scale phenomenon of the bed porosity was calculated by measuring the volume of the cell that was filled by a significantly large known mass of the granular material.

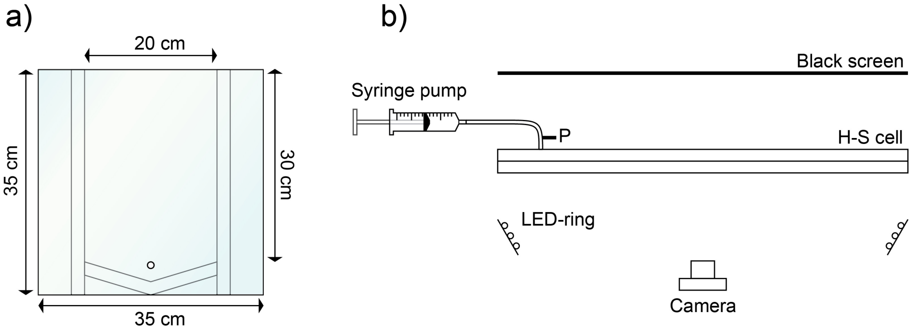

FIG. 1. a) Schematic of larger Hele-Shaw cell. b) Air is injected into Hele-Shaw cell via syringe pump to form fractures in a water-saturated, loose granular packing held in the cell with a gap size of 0.5 mm. Air pressure is recorded just before the inlet. $Q_{\text{pump}} = 0.01$ ml.min^{-1}, grains used for packing sieved to 0.20–0.25 mm, photo taken from below every 20 s.

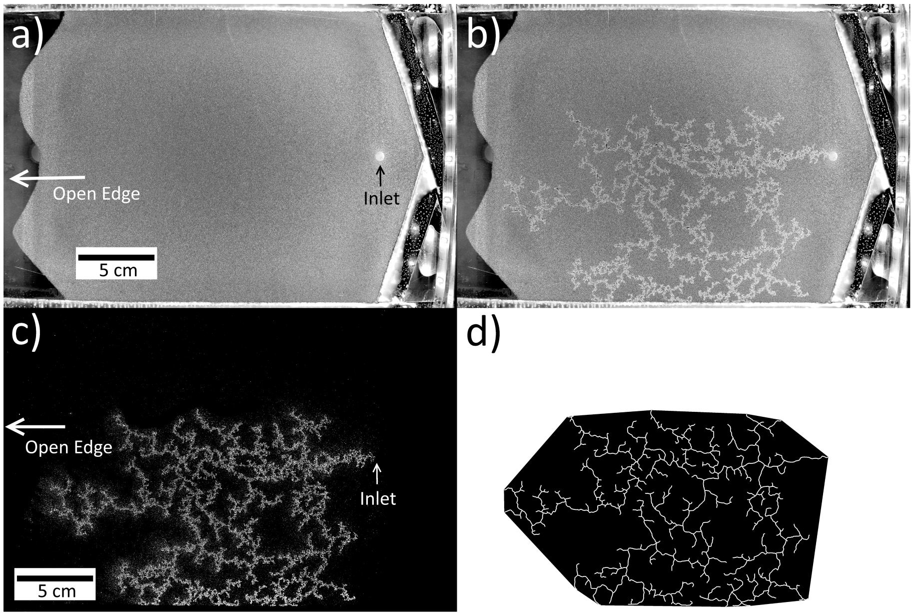

FIG. 2. Fracture invasion pattern in larger cell. a) Raw image of granular packing before gas invasion. b) Raw image of granular packing after gas has invaded forming a fracture pattern. c) The result of subtracting (a) from (b). d) Processed and skeletonised fracture path with its surrounding convex hull in black.

Fracture Pattern Image Analysis

The images taken during the experiment were used to investigate the overall pattern formed by the gas-driven fracture growth. The images were processed by a custom algorithm in MATLAB which subtracted them from an image taken of the initial bed before fracturing had occurred and then subjected them to thresholding, despeckling, closing operations, and skeletonisation to produce the fracture paths (Figure 2 (d)). The two-dimensional spatial density of the fracture patterns was calculated by dividing the skeletonised fracture length by the area of the convex hull of the pattern (the area occupied by a perimeter defined by straight lines between it's most extreme points), see Figure 2 (d).

High-speed Setup

A smaller Hele-Shaw cell was constructed for close-up high-speed imaging to reduce the chance of fractures growing off camera, see Figure 3. Two 150x150x10 mm^3 glass plates were held apart by impermeable plastic adhesive spacers of 0.9 mm thickness, defining the cell gap. Like the larger cell, the cell was left open at one end and the resultant channel formed was 100 mm wide and 125 mm long. A syringe needle was inserted through the plastic spacer, reaching 25 mm into the cell opposite the open end. The needle tip formed the air inlet, driven by a syringe pump (Harvard Scientific, PHD Ultra) at constant injection rate of $Q_{\text{pump}} = 0.01$ ml.min^{-1} with a reservoir volume $V_{\text{gas}} = 8$ ml.

Glass beads (0.20–0.25 mm) were used to form a granular packing as described for the larger cell, leaving a 10 mm water filled gap at the open edge. However, an initial layer of smaller 0.10-0.15 mm beads was first deposited in the cell to form a low-permeability zone at the bottom of the channel next to the syringe needle. This was done to prevent the fractures from growing back along the needle and along the bottom edge of the cell outside of the filmed area, since edge effects between the larger grains and the syringe needle create a high permeability zone compared with the rest of the bed.

The high-speed camera (Photron Fastcam 1024-PCI) had a resolution of 1024x1024 pixel^2, and was set to film a 50x50 mm^2 area of the Hele-Shaw cell channel with a frame rate of 1000 fps. This 50x50 mm^2 frame was large enough to capture all motion of the granular bed in the vicinity of an individual fracture event. The longest fracture event observed lasted for 1 s and the shortest for 0.13 s.

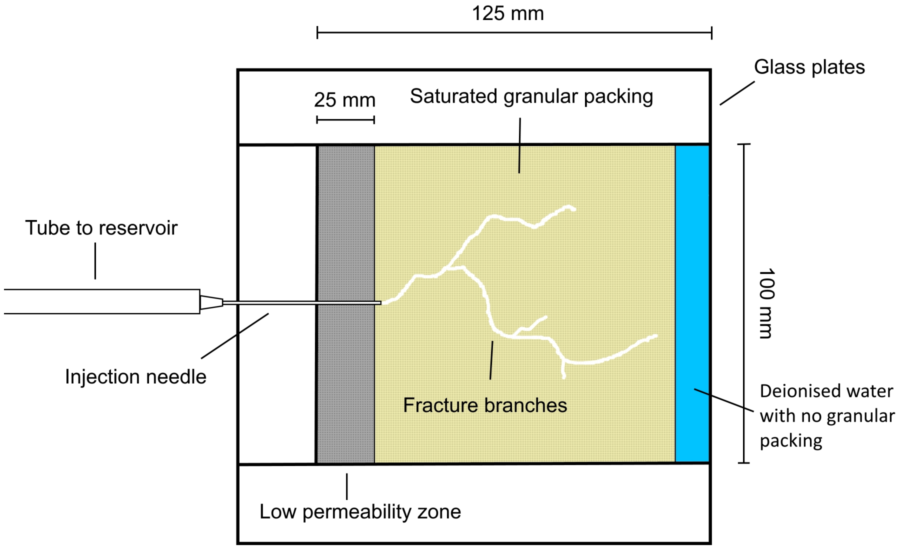

FIG. 3. Small Hele-Shaw cell. Air is injected through a syringe needle to form fractures in a water-saturated, loose granular packing held in the cell with a gap size of 0.9 mm. $Q_{\text{pump}} = 0.01$ ml.min^{-1}, grains used for packing sieved to 0.20–0.25 mm, grains used in low permeability zone sieved to 0.10–0.15 mm, high-speed camera filmed from below at 1000 fps.

High-speed Image Analysis

The videos taken with the high-speed camera were used to investigate the deformation and motion of the granular packing around individual fractures. Displacement and velocity vector fields of the granular motion were found using Particle Image Velocimetry (PIV) performed using Ncorr, a MATLAB based digital image correlation (DIC) software ([1]). PIV is a process in which sub-windows of an image are cross-correlated with sub-windows of another image taken at a later time to obtain displacement vectors $\vec{S}(x, y) = X(x, y)\vec{i} + Y(x, y)\vec{j}$ located at (x, y) positions in the initial image. These displacement vectors are then calibrated with the distance across each sub-window (0.15 mm) and the time between images (1 ms) to obtain the displacement and velocity vector fields.

The average velocity profile of the filmed fracturing events presented here was found using a custom MATLAB algorithm that selected frames from a high-speed video in which the PIV data contained a minimum threshold of movement, an average mean motion of 0.5 mm.s^{-1} in the 50x50 mm^2 frame was found to appropriately select frames with active fracture growth. Those velocity fields depicting growth were then re-centred to the location of their fracture tip, which was reliably found by correlating the directions of the largest 50 vectors in the frame to find their overlapping point of origin, defined here as the fracture tip. This method relies on the observation that the deformation field spreads out approximately radially from the tip of the fracture. These translated fields were then rotated to the same vertical orientation by determining their overall angles of motion, which was found by the mean angle of those same 50 largest vectors, defined here as the direction of fracture growth. The PIV data found at this fracture tip was used to find the fracture tip speed for that frame. 783 processed velocity fields from multiple fracturing events were averaged to find the contour plot presented in Figure 8 later in Section 3.

Compaction of the granular medium around fracture growth was calculated in a custom algorithm in MATLAB with a larger sub-window (0.58 mm), to enable the cross-correlation of multiple grains at once, using the following equation

$$\Xi = (\Delta X_i \;+\; \Delta Y_j) \,.\, \frac{100}{L}, \tag{1}$$

where Ξ is the percentage of compaction relative to the original packing, ΔX_i is the difference between the $\vec{i}$ components of the displacement vectors found on the left and right sides of the sub-window, ΔY_j is the difference between the $\vec{j}$ components of the displacement vectors found above and below the sub-window, and L is the length across the sub-window.

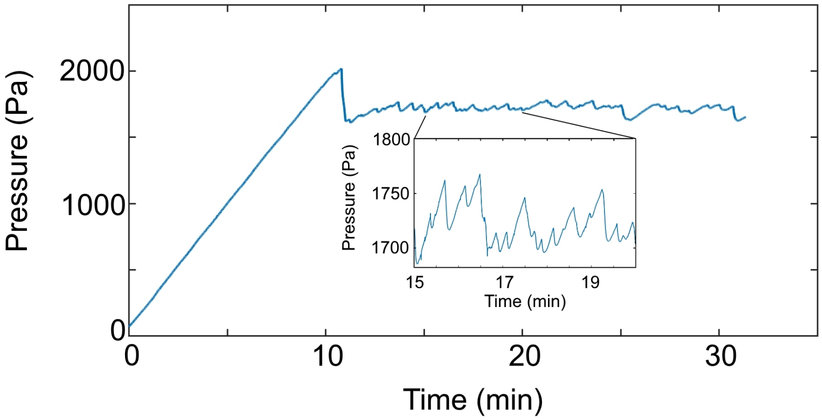

FIG. 4. Air pressure curve during gas-driven fracturing of saturated granular media in the large cell. The initial linear increase is a result of gradual compression of air at steady pump rate prior to fracturing. The first sudden drop corresponds to the first invasion through the inlet. Thereafter, the gas pressure displays a saw-tooth shape where the peaks correspond to the pressure required to initiate a new fracture, the local pressure minima correspond to the end of a fracture growth event, and the steady increase correspond to the ”stick” period between fracture events, where the gas compresses at the rate dictated by the pump. Inset: Subsection of curve, illustrating the saw-tooth shape of the pressure during stick-slip fracture growth. (Injection rate q = 0.01 ml.min^{-1}, 0.20–0.25 mm beads.)

RESULTS AND DISCUSSION

Fracture Pattern

This section outlines the features of the patterns formed by pneumatic fracture growth in a deformable saturated granular media in the large cell described in Section 2.1. Figure 2 b) shows an example image of an invasion pattern in this setup, while (d) shows the skeletonised path of the pattern that was used for analysis. As the air invades the saturated packing it creates fracture pathways that branch by tip-splitting. The resultant fracture pattern forms a maze: a branching, loopless, binary tree-like structure. The reason for the self-avoiding nature of the fracture network cannot be discerned from the images alone and will be examined using PIV in a later section.

Figure 4 presents the recorded air pressure as a function of time corresponding to the experiment in Figure 2. Initially, the pressure increases at a constant rate as the air is compressed by the steady pump rate (0.01 ml.min^{-1}). Eventually the pressure reaches a required threshold (1720 Pa on average) to penetrate the water-grain packing, marked by a pressure drop as the air expands to fill the growing fracture. Once the pressure stored in the invading gas drops low enough that the friction in the granular packing can hold it back (1680 Pa on average), the fracture growth stops and the pressure begins to build again. (Note that the first peak is larger than the subsequent saw-tooth pattern because of the influence of the inlet during the filling process.) This kind of irregular saw-tooth pressure evolution is characteristic of stick-slip frictional processes, indicating that it is the grain-grain and grain-cell friction that holds back the invading gas until the threshold pressure is reached.

It is also important to note that unlike viscous fingering, the growth is not directional or channelled into dominant pathways but instead appears random in its orientation and selection of nucleation point. However, the fracture branches do tend to grow together to fill the local space around previously made branches. It was observed that one fracture event would often trigger events in other local branches, likely as the result of a flow-induced disturbance in the packing caused by the initial growth ([2]).

Growth of a single fracture

As air invades the water-saturated granular packing, capillary forces at the interface impose a force on the grains, eventually overcoming the opposing friction from the granular bed. The air-water interface pushes the grains aside to form an air-filled cavity in the shape of a fracture. A close-up image of a section of a fracture length is shown in Figure 5. The fracture shape is irregular and the width of the fracture space varies. The widest sections measure around 5–10 bead diameters (1–3 mm), while at the narrowest, the fracture aperture is indistinguishable from the surrounding granular packing.

Figure 6 (a) examines the speed of the fracture tip, calculated with PIV data from high-speed images, as it penetrates the granular packing in the smaller cell during a single recorded fracturing event that lasted for approximately 1 s. For more than 10 s before and after the event there was no granular motion observed anywhere in the cell. The highest measured tip speed during the event was recorded for its initial motion at 54 mm.s^{-1} for approximately 0.01 s, the next three bursts of motion all

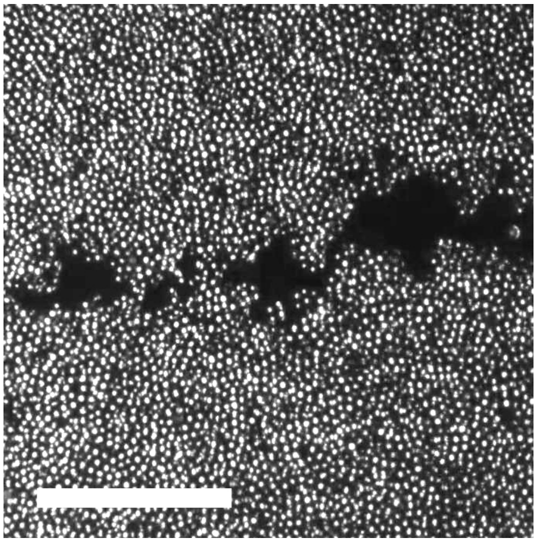

FIG. 5. Close-up image of a gas-filled fracture cavity in a water-saturated granular packing in the small Hele-Shaw cell. Scale bar: 5 mm.

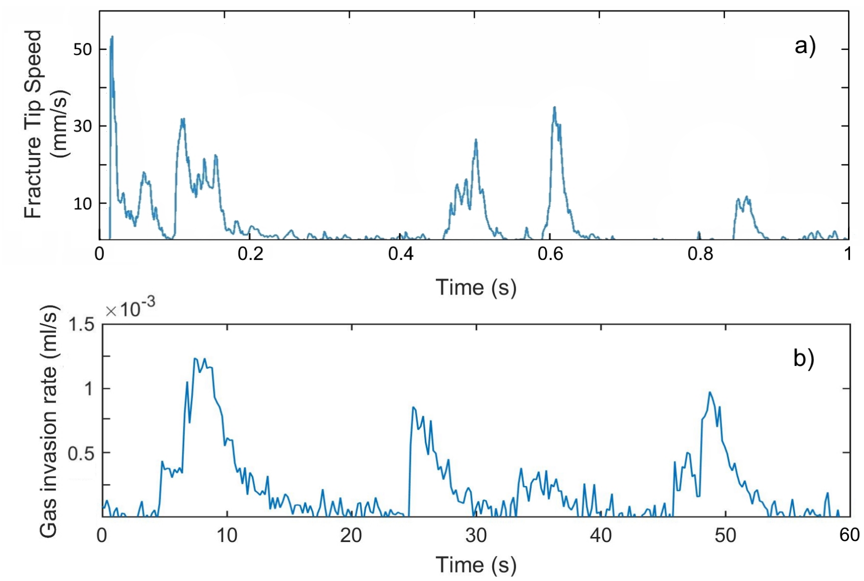

FIG. 6. Intermittent motion at different scales. a) Shows the speed of the fracture tip during a fracturing event that lasted for 1 s. b) Shows a section (minute 19) of the gas invasion rate for Figure 4 for a period of 1 minute.

had peak speeds of around 30 mm.s^{-1}, lasting approximately 0.06, 0.05, and 0.03 s, while the final period of motion displayed a lower tip speed of 11 mm.s^{-1} for approximately 0.03 s. This evidences that there is intermittency in the granular behaviour of fracture growth, with five distinct periods of motion separated by brief pauses during one event, where one event is equivalent to one pressure drop in Figure 4. This intermittent behaviour was observed in all the recorded fracturing events.

Note that there are two scales of intermittency at work here. The first, that has already been observed in previous work ([2]), is in the larger scale stick-slip nature of the fracture pattern formation demonstrated by the saw-tooth pressure curve in Figure 4. Fracture growth is signalled by sharp drops in pressure due to air expansion, and over a 20 minute period there are approximately 48 large and small pressure drops that can clearly be distinguished, giving an average time of 25 s between these main fracture events. The second scale of intermittency is in the stick-slip nature of the granular motion within individual fracturing events captured by the high-speed camera and exemplified in Figure 6 (a), with five individual periods of motion taking place in the space of about 1 s.

From the pressure signal recorded using the large Hele-Shaw cell we can infer the rate of gas invasion into the granular-liquid mixture. Using Boyle's law $P_0\Delta V \approx -V_{\text{gas}}\Delta P$, where P_0 is ambient pressure, and we have assumed small volume and pressure changes, ΔV and ΔP respectively, during fracturing as well as ideal gas behaviour at constant temperature, we have a volumetric gas invasion rate during fracture growth:

$$Q_{\text{gas}} = \frac{\Delta V}{\Delta t} = -\frac{\Delta P}{\Delta t}\frac{V_{\text{gas}}}{P_0} + Q_{\text{pump}}. \tag{2}$$

Figure 6 (b) shows Q_{gas} plotted as a function of time over a one minute time duration where each fracture event recorded with low time resolution in the large Hele-Shaw cell appears as an individual peak. The high-speed camera results in Figure 6 (a) demonstrate that what appears as one single, large-scale, fracture event is in fact composed of several smaller stick-slip motions which are separated by fractions of a second.

Given that each rise and fall of the gas invasion rate in Figure 6 (b) corresponds to one fracturing event in the larger cell, it would be expected that the period of time that it lasts for would be similar to the total length of time for which an aggregated fracturing event lasts for in the smaller cell as seen in Figure 6 (a). However, the events in Figure 6 (b) last for up to 10 s, compared with 1 s in Figure 6 (a). There are a couple of explanations for this discrepancy. First is that, as mentioned previously, fracturing events in the larger cell often trigger more events in other branches, causing the period of fracturing to last longer. The smaller cell was made to specifically minimise this effect. Second is that when the invading gas was not fracturing it would frequently evacuate water from pore spaces around fracture branches via capillary invasion, i.e. without any motion in the grains. These small invasions likely also occur before, during, and after fracture growth, increasing the time duration of the fracture events as inferred from the pressure data, as well as resulting in minor instances of invasion between fracture events, explaining the minor peaks in Figure 6 (b) between the fracturing events. However, the meniscus of the water in the packing

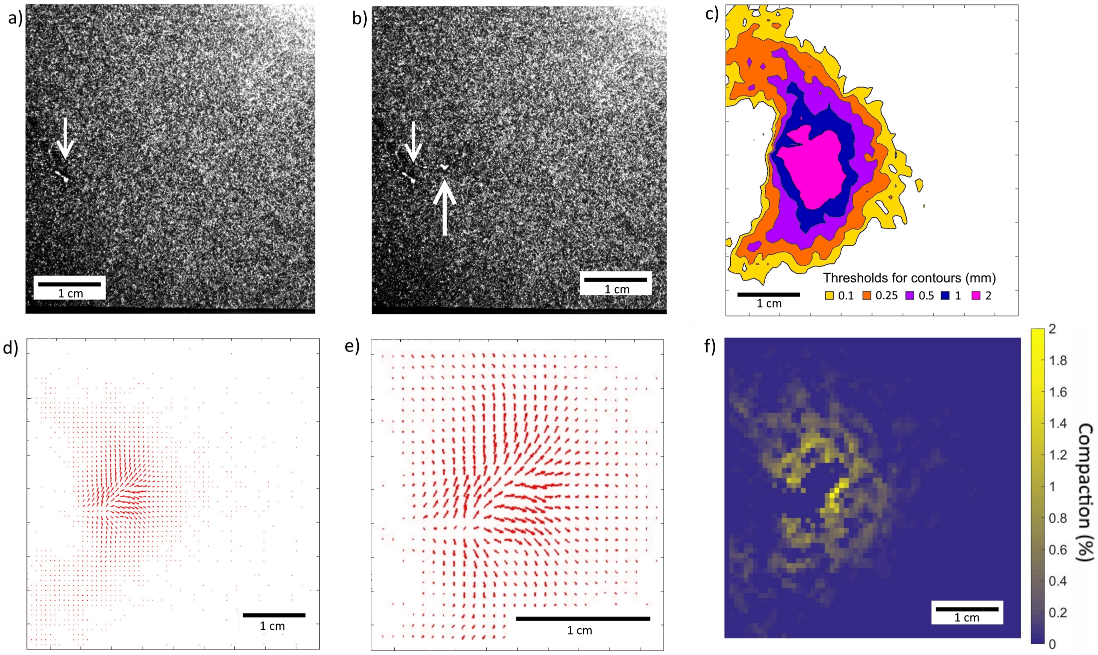

FIG. 7. Example of granular motion during fracturing. a) Raw video frame before a fracturing event takes place. b) Raw video frame after a fracture event that lasted 0.13 s (initial arrow points to original fracture cavity, while the second points to the new fracture cavity). c) Contour plot of displacement field for grains over the fracturing event. d) Velocity vectors for (c) showing the direction of granular motion. e) Zoom in of plot of d) on the fracture cavity. f) Compaction relative to initial packing fraction as a result of the deformation caused by grain displacement field during fracturing.

(the interface between water and the advancing gas) could not be seen in the high-speed imaging, and so all of the PIV analysis presented is representative of the granular motion only, with no capillary invasion being observable or recorded in our data.

Deformation of the granular bed

We studied the granular motion during fracture growth by determining the displacement profiles of the grains as the invading gas deformed the packing. For example, Figure 7 (a) shows the raw image of the packing before a fracturing event while Figure 7 (b) shows it after. The fractures are rather small at this scale, however looking at the overall displacement contour profile for this event in Figure 7 (c) reveals that the deformation caused is considerably wider than the fracture itself. Some of the minimally disturbed grains, moving at least 0.1 mm, are up to 26 mm away from the parent fracture, and the region of the most disturbed grains surrounding the fracture, moving at least 2 mm, has a radius of approximately 8 mm compared to the widest point of fracture width of 0.7 mm. Though the influence of the fracture growth is pronounced on a surrounding area that is at least an order of magnitude larger than the fracture width itself, it quickly drops off and remains local to the vicinity of the active fracture.

The compaction relative to the undisturbed packing as a result of that fracture event is presented in Figure 7 (f) where the compaction is found to peak at 1.9 % and average at 0.5 %. For reference, the compaction of a random loose packing of spheres by 2–5 % is equivalent to a bed being vibrated into close packing ([9]). The shape of the compacted area mimics the shape of the displacement profile, compacting most significantly on the sides and in front of the fracture path and then significantly dropping off further away from the fracture. The resolution of the sub windows in the compaction PIV data is insufficient to resolve the width of the gas filled fracture, leading to the exaggerated size of the fracture width.

In both the displacement and compaction profiles it can be seen that the granular disturbance is avoiding the region behind the fracture's origin. This area holds the previous fracture branch (which can be seen in Figure 7 (a)), as well as its previously compacted material. The compaction of the granular material causes narrowing of pore throats, leading to increased capillary invasion pressures along the fracture interface. The compacted front also has a high frictional resistance to motion due to stress dispersion to the confining plates. This is why subsequent granular motion avoids these zones and the gas invasion initially proceeds through pore spaces without mobilising grains. The invading gas needs to escape the compacted zone around the parent fracture cavity before it can create a new cavity where grains are still free to be moved.

To obtain a broader picture of this granular motion, the PIV data of 783 images of active fracture growth from multiple

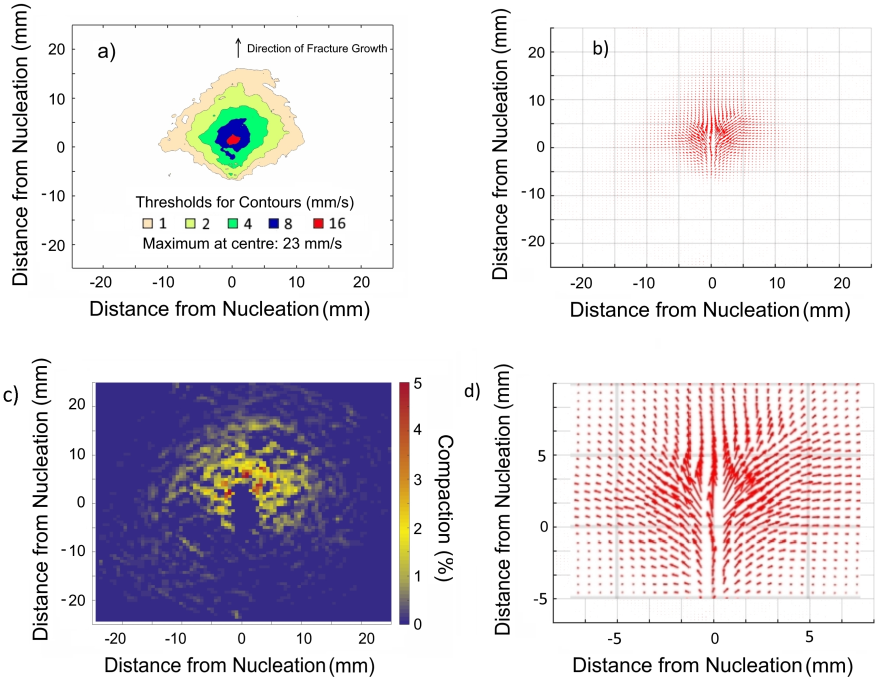

FIG. 8. Average granular motion. a) Average velocity profile of grains with respect to distance from the point of nucleation during fracture growth, calculated using 783 PIV fields from 1 ms video frames of multiple fracture events. b) Velocity vectors for (a) showing the direction of granular motion during fracturing. c) Average compaction profile of grains caused by fracture growth with respect to distance from the point of nucleation calculated using Equation 1. d) Zoom in of plot of b) on the nucleation point.

fracturing events were processed and averaged to form the velocity profile presented in Figure 8. The overall profile illustrates that granular motion is mostly in the direction of growth and to either side of its point of nucleation in the centre of the figure. The notable valley, or pinch in the profile behind the point of nucleation is the result of the previous fractures influence on the packing preventing motion. The majority of velocity profile is a halo of minor movement (less than 4 $\mathrm{mm.s}^{-1}$) surrounding the nucleation point approximately 5 mm in all directions. The centre of the profile shows the average maximum velocity of the grains to be 23 $\mathrm{mm.s}^{-1}$. This velocity is relatively rapid for grains of radius 0.2 mm, but the individual grains move for approximately 0.1 s as the invading gas front advances past them, resulting in a displacement of only around 2 mm (see Figure 7). Away from the nucleation point the velocity of the grains rapidly decreases as the motion is dispersed among the granular material. This dispersal of motion is only possible because the grains begin in a random loose packing, with room to be compacted further.

Compaction Fronts as a Constraint on Pattern Formation

The air pressure applies a stress on the interfacial grains that disperses through grain-grain contacts in the compacted region surrounding the fracture. Some of the granular stress is redirected to the confining wall of the cell, increasing the frictional resistance needed to be overcome to expand the fracture. A new fracture will expand to a maximum width such that the friction from the compacted zone balances the air pressure at the fracture wall ([2]). The compaction data calculated from the PIV data is displayed in Figure 8 and reveals a halo of compaction around the fracture nucleation point in the direction of its growth.

Figure 9 displays the percentage of compaction relative to the undisturbed packing as a function of distance from the point of nucleation in the direction of growth (yellow), 90^o from the direction of growth (blue), and -90^o from the direction of growth (red). Here it can be seen that either side and in front of the fracture nucleation point are regions of marked increase in compaction. The peak of the compaction zones on either side are 1.6 and 1.8 % with both occurring at 3.4 mm from the point of fracture growth, and each rapidly fall to half of their peak at approximately 4 mm from the origin. The compaction zone in the direction of growth is notably larger with a peak of 4.8 % occurring at 5.4 mm from the point of fracture growth, and falls to half its peak value at approximately 7 mm from the origin. The larger compaction in the direction of growth is not surprising, and can help explain the branching meandering path the fractures take through the packing since the grains to either side are always more free to move than those directly ahead.

The formation of a compaction zone around fracture growth explains two notable phenomena in three-phase fracturing. First,

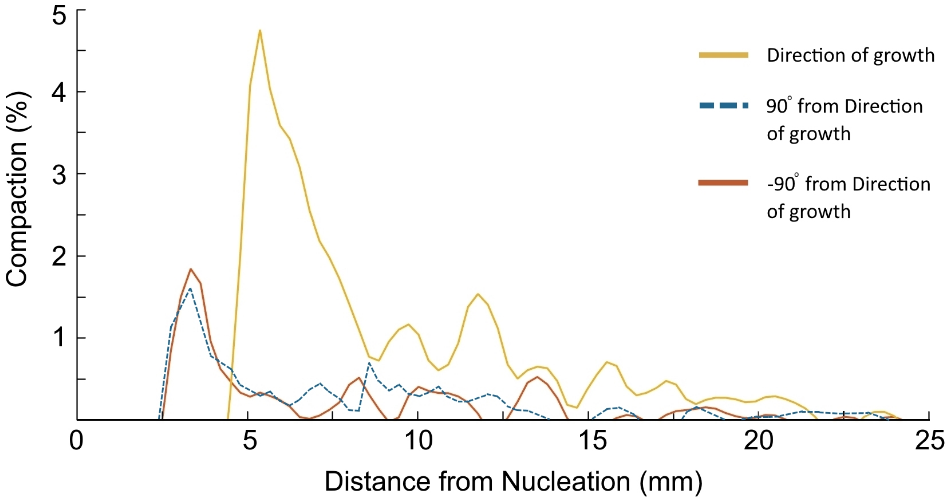

FIG. 9. Compaction of the granular packing as a function of distance from the fracture nucleation point in the direction of growth (solid line with largest peak), 90^o from the direction of growth (dashed line), and -90^o from the direction of growth (other solid line).

the narrow pore sized necks that form before each fracture cavity occur because the air must invade an area that has already been compacted by a previous fracture event; since it can hardly move the grains it invades through pores until it reaches grains that are less compacted, where it can then expand into a new cavity and subsequently form a new surrounding compaction zone. Second, with each fracture branch having a compaction zone around it, the structure of the pattern in larger Hele-Shaw geometries will self-avoid. The fractures cannot grow into already compacted regions, and seek out undisturbed material.

If we imagine two fractures that have grown parallel to each other as close as possible, they will be separated by a distance equal to each of their compaction fronts aligned on that side and half of each of their fracture widths, as illustrated in Figure 10. Simply put, the width of space occupied by a fracture and its compaction fronts, that no other fracture can then approach is:

$$O_w = W + 2L, \tag{3}$$

where O_w is the total occupied width of a fracture and its fronts, W is the fracture's internal width, and L is the width of a compaction front. Using the point at which compaction drops to below half of its peak as boundary of the compaction zone, with Figure 9 we can determine that $0.5W + L$ is on average 4 mm for these experiments, giving an estimated O_w value of 8 mm. As such, we would expect that a fracture pattern in this system would always form with fractures at a minimum of that distance apart. Fracture branches might grow further away from each other than that, but they can grow no closer.

In the larger cell we see that the invading gas seeks out undisturbed regions of the packing, producing a pattern that tends to locally fill the space of the system, with branches being separated by this O_w length scale. For example, the average distance between fractures in Figure 2 (d) and other patterns made in the same system is 9 mm. This is in good agreement with our calculated estimate of 8 mm and is likely larger because the fractures will not all conveniently grow parallel to each other. Another useful way to describe this phenomena is that, given the gas-driven fractures will eventually grow to space-fill a system, the inverse of the O_w value (in units of cm) is the average number of fractures encountered when moving 1 cm in any direction from a point in the completely fractured packing. Thus, an approximate spatial density of the fracture pattern can be defined as:

$$D = \frac{1}{O_w} = \frac{1}{W + 2L}, \tag{4}$$

where D is the spatial density of the fracture pattern. In this case the spatial density of the patterns is 1.1 cm^{-1}, while our upper limit derived from the compaction front data is 1.3 cm^{-1}.

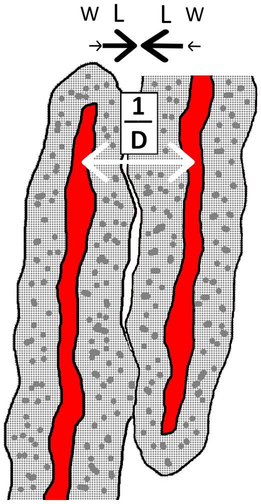

FIG. 10. Illustration of two parallel fracture cavities (enclosed filled areas) and their touching compaction fronts (surrounding speckled areas). The distance made up from the fracture widths (W) and their compaction fronts (L) keeps the fractures a minimum set distance apart that is equivalent to the inverse of their spatial density (1/D).

CONCLUSION

We have used close-up, high-speed imaging to analyse the motion of cohesionless grains during the formation of fracture cavities as a result of a loose granular packing saturated with water being subjected to a forced invasion of air. The observed sub-millimetre and microsecond scale events were examined in the context of, and were compared to, the larger scale observation of fracture patterns in a Hele-Shaw cell that are defined by a characteristic length scale.

In concordance with earlier studies ([4, 6, 10, 11, 16, 17, 24, 27]), a network of conductive pathways in the shape of fractures is observed. As the pressure in the system builds, the capillary and viscous forces eventually overcome frictional resistance of the grains and fractures are forced open, relieving the pressure in the invading gas. This process then repeats resulting in stick-slip intermittent growth. The fracture branches avoid each other when branching, but yet still remain relatively local as their nearby deformations in the packing stimulate local growth.

Studying the growth of individual branches with high-speed video revealed other scales of intermittency during fracture growth. Fractures were seen to have frictional behaviour within fracturing events, with the fracture tip speed varying and pausing in its own stick-slip manner (Figure 6). The gas front was regularly observed to invade through pore spaces while the surrounding packing remained static, indicating that the immediate grains were resistant to motion while a fracture cavity could be formed in those found further along the invasion path. PIV analysis of the high-speed imaging of multiple fracturing events allowed us the generate an average velocity profile for fracture growth (Figure 8). This profile shows the wide influence of the deformation caused by fracturing in comparison to the size of the fracture. The shape of the velocity profile revealed regions behind and to either side of the point of growth that granular motion avoids as a result of deformation cause by the previous fracture. As such, a compaction profile was also generated, displaying the halo of compaction around the fracture growth. This explains why the gas first invades through pores spaces before mobilising grains beyond its previous compaction front, why the fractures self-avoid in the larger scale pattern forming process, and allows us to calculate the upper limit for the spatial density for fracture patterns in these circumstances.

Geological phenomena such as sedimentary methane venting, magma degassing, and soil drying are known to incorporate processes involving gas-driven fracturing of saturated packings and granular suspensions, and as such our techniques and results can contribute to an improved understanding of their resultant fracture network properties and the three-phase gas, liquid, and grain interactions that cause them ([13, 18, 21, 29, 30]). In addition, being able to predict spatial density of fracture patterns in saturated granular material is particularly relevant in engineering applications such as stimulating hydrocarbon reservoirs and soil remediation where increasing the permeability of a bulk granular material with fracture networks can greatly increase efficiency of fluid exchange ([7, 12, 22]).

Overall, the techniques and results presented here illustrate that multiphase fracturing in saturated granular material is even more complex than previously thought, with relevant phenomena occurring across multiple length and time scales over different orders of magnitude. Future work can be directed into multiple avenues of questioning: is it possible to observe the motion of the water meniscus during fracturing events and would doing so help explain the branching process in the invasion pattern; can these fractures be studied in a fully 3D system and are the resultant invasion patterns also dominated by compaction fronts; how does changing the interstitial or invading fluids affect the dynamics observed here; and can varying the properties of the packing to make heterogeneous layers be used to model these processes in sedimentary systems.

Acknowledgements

We thank James Campbell for discussions. This work was supported in part by the Engineering and Physical Sciences Research Council (EP/L013177/1) and Sêr Cymru National Research Network in Advanced Engineering and Materials (NRN141).

---

* b.sandnes@swansea.ac.uk

[1] Blaber, J., Adair, B., and Antoniou, A., Ncorr: Open-source 2d digital image correlation matlab software, *Experimental Mechanics*, vol. **55**, no. 6, pp. 1105–1122, 2015.

[2] Campbell, J.M., Ozturk, D., and Sandnes, B., Gas-driven fracturing of saturated granular media, *Phys. Rev. Applied*, vol. **8**, p. 064029, 2017.

[3] Cavanagh, A.J. and Haszeldine, The sleipner storage site: Capillary flow modeling of a layered co2 plume requires fractured shale barriers within the utsira formation, *Int. J. Greenh. Gas Control*, vol. **21**, pp. 101–112, 2014.

[4] Chevalier, C., Lindner, A., and Clément, E., Destabilization of a Saffman-Taylor fingerlike pattern in a granular suspension, *Phys. Rev. Lett.*, vol. **99**, no. 17, p. 174501, 2007.

[5] Chevalier, C., Lindner, A., Leroux, M., and Clément, E., Morphodynamics during air injection into a confined granular suspension, *J. NonNewton. Fluid*, vol. **158**, no. 1, pp. 63–72, 2009.

[6] Choi, J.H., Seol, Y., Boswell, R., and Juanes, R., X-ray computed-tomography imaging of gas migration in water-saturated sediments: from capillary invasion to conduit opening, *Geophys. Res. Lett.*, vol. **38**, no. 17, 2011.

[7] Christiansen, C.M., Riis, C., Christensen, S.B., Broholm, M.M., Christensen, A.G., Klint, K.E.S., Wood, J.S.A., Bauer-Gottwein, P., and Bjerg, P.L., Characterization and quantification of pneumatic fracturing effects at a clay till site, *Environ. Sci. Technol.*, vol. **42**, no. 2, pp. 570–576, 2008.

[8] Cras, J., Rowe-Taitt, C., Nivens, D., and Ligler, F., Comparison of chemical cleaning methods of glass in preparation for silanization, *Biosensors and Bioelectronics*, vol. **14**, no. 8, pp. 683 – 688, 1999.

[9] Dullien, F.A.L., *Porous media: fluid transport and pore structure*, Academic press, 2012.

[10] Eriksen, F.K., Toussaint, R., Turquet, A.L., Måløy, K.J., and Flekkøy, E.G., Pneumatic fractures in confined granular media, *Physical Review E* , vol. **95**, no. 6, p. 062901, 2017.

[11] Fauria, K.E. and Rempel, A.W., Gas invasion into water-saturated, unconsolidated porous media: implications for gas hydrate reservoirs, *Earth Planet. Sc. Lett.*, vol. **312**, no. 1, pp. 188–193, 2011.

[12] Frank, U. and N., B., Remediation of low permeability subsurface formations by fracturing enhancement of soil vapor extraction, *J. Hazard. Mater.*, vol. **40**, pp. 191–201, 1995.

[13] Goehring, L., Conroy, R., Akhter, A., Clegg, W.J., and Routh, A.F., Evolution of mud-crack patterns during repeated drying cycles, *Soft Matter*, vol. **6**, no. 15, pp. 3562–3567, 2010.

[14] Hele-Shaw, H.S., On the motion of a viscous fluid between two parallel plates, *Nature*, vol. **58**, pp. 34–36, 1898.

[15] Holtzman, R. and Juanes, R., Crossover from fingering to fracturing in deformable disordered media, *Phys. Rev. E*, vol. **82**, p. 046305, 2010.

[16] Holtzman, R., Szulczewski, M.L., and Juanes, R., Capillary fracturing in granular media, *Phys. Rev. Lett.*, vol. **108**, no. 26, p. 264504, 2012.

[17] Islam, A., Chevalier, S., Salem, I.B., Bernabe, Y., Juanes, R., and Sassi, M., Characterization of the crossover from capillary invasion to viscous fingering to fracturing during drainage in a vertical 2D porous medium, *Int. J. Multiphase Flow*, vol. **58**, pp. 279–291, 2014.

[18] Kitsunezaki, S., Crack growth in drying paste, *Adv. Powder Technol.*, vol. **22**, no. 3, pp. 311–318, 2011.

[19] Knudsen, H.A., Sandnes, B., Flekkøy, E.G., and Måløy, K.J., Granular labyrinth structures in confined geometries, *Phys. Rev. E*, vol. **77**, no. 2, p. 021301, 2008.

[20] Løvoll, G., Méheust, Y., Toussaint, R., Schmittbuhl, J., and Måløy, K.J., Growth activity during fingering in a porous Hele-Shaw cell, *Phys. Rev. E*, vol. **70**, no. 2, p. 026301, 2004.

[21] Oppenheimer, J., Rust, A.C., Cashman, K.V., and Sandnes, B., Gas migration regimes and outgassing in particle-rich suspensions, *Front. Phys.*, vol. **3**, no. 60, 2015.

[22] Rogala, A., Krzysiek, J., Bernaciak, M., and J., H., Non-aqueous fracturing technologies for shale gas recovery, *Physicochem. Probl. Miner. Process.*, vol. **49**, no. 1, pp. 313–322, 2013.

[23] Saffman, P.G., Viscous fingering in Hele-Shaw cells, *J. Fluid Mech.*, vol. **173**, pp. 73–94, 1986.

[24] Sandnes, B., Flekkøy, E.G., Knudsen, H.A., Måløy, K.J., and See, H., Patterns and flow in frictional fluid dynamics, *Nat. Comm.*, vol. **2**, p. 288, 2011.

[25] Sandnes, B., Flekkøy, E.G., and Måløy, K.J., Stick slip displacement of confined granular mixtures: bubble expansion, *Eur. Phys. J.-Special Topics*, vol. **204**, no. 1, pp. 19–25, 2012.

[26] Sandnes, B., Knudsen, H.A., Måløy, K.J., and Flekkøy, E.G., Labyrinth patterns in confined granular-fluid systems, *Phys. Rev. Lett.*, vol. **99**, no. 3, p. 038001, 2007.

[27] Shin, H. and Santamarina, J.C., Fluid-driven fractures in uncemented sediments: underlying particle-level processes, *Earth Planet. Sc. Lett.*, vol. **299**, no. 1, pp. 180–189, 2010.

[28] Tallakstad, K.T., Knudsen, H.A., Ramstad, T., Løvoll, G., Måløy, K.J., Toussaint, R., and Flekkøy, E.G., Steady-state two-phase flow in porous media: statistics and transport properties, *Phys. Rev. Lett.*, vol. **102**, no. 7, p. 074502, 2009.

[29] Varas, G., Vidal, V., and Geminard, J.C., Venting dynamics of an immersed granular layer, *Phys. Rev. E*, vol. **83**, p. 011302, 2011.

[30] Weinberger, R., Evolution of polygonal patterns in stratified mud during desiccation: the role of flaw distribution and layer boundaries, *Geol. Soc. Am. Bull.*, vol. **113**, no. 1, pp. 20–31, 2001.